LAWRENCE
LIVERMORE
NATIONAL
LABORATORY

LLNL-JRNL-411605

A crust and upper mantle model of Eurasia and North Africa for Pn travel time calculation

S. Myers, M. Begnaud, S. Ballard, M. Pasyanos, W. S. Phillips, A. Ramirez, M. Antolik, K. Hutchenson, J. Dwyer, C. Rowe, G. Wagner

March 27, 2009

Bulletin of the Seismological Society of America

Disclaimer

A crust and upper mantle model of Eurasia and North Africa for Pn travel time calculation

Stephen C. Myers[1], Michael L. Begnaud[2], Sanford Ballard[3], Michael E. Pasyanos[1], W. Scott Phillips[2], Abelardo L. Ramirez[1], Michael S. Antolik[4], Kevin D. Hutchenson[4], John J. Dwyer[5], Charlotte A. Rowe[2], and Gregory S. Wagner[5]

[1] Lawrence Livermore National Laboratory
[2] Los Alamos National Laboratory
[3] Sandia National Laboratories
[4] Quantum Technology Sciences, Inc.
[5] Air Force Technical Applications Center

Corresponding author: **Stephen C. Myers**
L-046
Lawrence Livermore National Laboratory
Livermore, CA 94550
(925) 423-4988

Submitted to Bulletin of the Seismological Society of America
July 29, 2009
Revised 10/1/09
Accepted 10/9/09

LLNL-JRNL-411605

Abstract

We develop a Regional Seismic Travel Time (RSTT) model and methods to account for the first-order effect of the three-dimensional crust and upper mantle on travel times. The model parameterization is a global tessellation of nodes with a velocity profile at each node. Interpolation of the velocity profiles generates a 3-dimensional crust and laterally variable upper mantle velocity. The upper mantle velocity profile at each node is represented as a linear velocity gradient, which enables travel time computation in approximately 1 millisecond. This computational speed allows the model to be used in routine analyses in operational monitoring systems. We refine the model using a tomographic formulation that adjusts the average crustal velocity, mantle velocity at the Moho, and the mantle velocity gradient at each node. While the RSTT model is inherently global and our ultimate goal is to produce a model that provides accurate travel time predictions over the globe, our first RSTT tomography effort covers Eurasia and North Africa, where we have compiled a data set of approximately 600,000 Pn arrivals that provide path coverage over this vast area. Ten percent of the tomography data are randomly selected and set aside for testing purposes. Travel time residual variance for the validation data is reduced by 32%. Based on a geographically distributed set of validation events with epicenter accuracy of 5 km or better, epicenter error using 16 Pn arrivals is reduced by 46% from 17.3 km (*ak135* model) to 9.3 km after tomography. Relative to the *ak135* model, the median uncertainty ellipse area is reduced by 68% from 3070 km^2 to 994 km^2, and the number of ellipses with area less than 1000 km^2, which is the area allowed for onsite inspection under the Comprehensive Nuclear Test Ban Treaty, is increased from 0% to 51%.

Introduction

Event location accuracy is vitally important to seismic monitoring because the location itself can provide insight about the event, and subsequent analysis – seismic and non-seismic – relies on an accurate location. Efforts to reduce magnitude thresholds in global monitoring systems have prompted the inclusion of regional seismic data into routine analysis. Regional seismic phases – broadly defined as the dominant phases at event-station distances less than 2000 km – work towards lowering thresholds because these waves are recorded more reliably than the teleseismic phases that are traditionally used for global monitoring. Unfortunately, the current practice in monitoring systems of using a one-dimensional (1-D, radially symmetric) Earth model as the primary means of computing travel times diminishes the utility of regional data, because prediction of regional travel times with a 1-D model is far less accurate than prediction of teleseismic travel times (*e.g.* Kennett et al., 1995; Yang et al., 2004; Flanagan et al., 2007). Reduced travel time prediction accuracy at regional distances results in degraded location accuracy when regional data are included (*e.g.* Bondár et al., 2004). If regional data are to be used for seismic monitoring, then travel time prediction error for regional phases must be reduced in order to avoid degradation of location accuracy and overall monitoring performance.

Teleseismic P-waves work well for monitoring larger events, because explosions generate large, impulsive P waves. Being the first arriving wave, P-wave arrival time is

easily measured because the onset is not complicated by the coda of other waves. Further, 1-D models (*e.g.* Jeffreys and Bullen, 1940; Herrin et al. 1968; Kennett and Engdahl, 1991; Kennett et al., 1995) can be used to predict teleseismic P-wave travel times with uncertainty of approximately 1 second, an error of less than ~0.3% of the total travel time. Accurate travel time prediction is achievable primarily because lateral heterogeneity in the lower mantle, where most of the teleseismic P-wave ray path resides and where the reaches maximum depth, is relatively weak. Also, computational error of travel times in a 1-D model is negligible because model symmetry affords a quasi-analytic solution (*e.g.* Buland and Chapman, 1983; Crotwell et al., 1999). Of particular importance to operational monitoring systems, 1-D models are easy to use. A table of travel time as a function of event-station distance and event depth can be pre-computed for each seismic phase. Phase-specific travel-time tables are universally applicable when used with a correction for station elevation and Earth ellipticity (Dziewonski and Gilbert, 1976), providing fast and simple travel-time retrieval.

The Pn phase is generally the first-arriving regional phase, making Pn the regional-distance analog of the teleseismic P phase. The Pn ray path resides predominantly in the shallow (depth<250 km) mantle. Unfortunately, a single 1-D model simply cannot capture the global variability of the crust and upper mantle structure. Crustal thickness can vary from approximately 5 km beneath oceans to more than 70 km beneath the highest mountains, and crustal and upper-mantle velocity can deviate from global averages by more than 10%. Empirically, travel time prediction error for the Pn phase is

2.0 to 2.5 seconds on average (~2% of the total travel time) and error can exceed 8 seconds in some regions (*e.g.* Engdahl et al., 1998; Flanagan et al., 2007).

Both empirical and model-based approaches have been used to improve regional travel time prediction. Empirical methods (Schultz et al., 1998; Myers and Schultz, 2000) interpolate travel time residuals from events with known or uncommonly accurate locations (ground-truth) to improve prediction accuracy. For empirical methods to be effective, ground-truth events must be well recorded at each station of the network. This condition may be met by long-standing networks and for limited geographic regions, such as former nuclear test sites. Empirical methods, however, do not provide global coverage, and travel time prediction accuracy at new monitoring stations gradually improves as new ground truth events are recorded.

Three-dimensional (3-D) regional models show promise for improving travel time prediction over broad areas (*e.g.* Johnson and Vincent, 2002; Ritzwoller et al., 2003; Yang et al., 2004; Morozov et al., 2005; Flanagan et al., 2007). Travel-time prediction using 3-D models typically involves pre-computing the travel time from a monitoring station to a volume of points, then – utilizing travel time reciprocity – the travel time from any point in the volume to that station can be interpolated. Travel-time lookup volumes have been demonstrated locally and at regional distance (*e.g.* Lomax et al., 2000; Johnson and Vincent, 2002; Flanagan et al., 2007). Because explosion monitoring is concerned with near-surface events, travel-time lookups have been simplified to a map of surface-focus corrections relative to a 1-D base model (*e.g.* Ritzwoller et al., 2002;

Yang et al., 2004; Morozov et al., 2005). Clearly, prediction error increases with event depth, and hundreds to thousands of station-phase specific correction surfaces must be managed in order to implement this approach. A collection of station-phase specific travel time lookups has been demonstrated, but a lookup approach adds considerable expense to the cost of maintaining a monitoring system. Model updates require re-computation and (most expensively) re-validation of each station-phase file. Lastly, current models of the crust and upper mantle have been shown to produce travel-time predictions that are biased with respect to the teleseismic P-wave calculations (Yang et al., 2004), necessitating an *ad hoc* travel time adjustment if regional and teleseismic data are to be used together.

We are developing a model framework and a method for calculating regional seismic travel times (RSTT) that can account for the first-order effects of crust and upper mantle heterogeneity. The model features a 3-D crust, including variable Moho depth and sediment thicknesses, and laterally variable mantle structure. As we describe below, a simplified model parameterization in the mantle – a linear velocity gradient – lends itself to real-time computation of Pn travel times, which is well suited for use in operational monitoring systems.

The RSTT model parameterization includes a global tessellation of nodes, making model coverage inherently global. Our ultimate plan is to produce a global model for universal computation of regional travel times. Achieving this goal requires development of a high-resolution global model of the crust and upper mantle. Working towards this goal, we

first report on the RSTT model parameterization and the method of travel time calculation for Pn. Secondary regional phases will be reported on in future publications. Below, we demonstrate RSTT Pn tomography and improvements in Pn travel time prediction and location accuracy across a broad sector of the globe that includes Eurasia and North Africa (Figure 1). This portion of the globe was chosen because of the excellent Pn path coverage for events with well-constrained locations. As a next step towards a the global RSTT model, we are in discussions with the U.S. Geological Survey about extending RSTT tomography to North America (Figure 1) and subsequently incorporating the RSTT method into the National Earthquake Information Center (NEIC) processing pipeline (R. Buland, personal communication).

Methods

Model Parameterization

We represent crust and upper mantle velocity structure using radial velocity profiles at geographically distributed nodes (Figure 2). The nodes form a triangular tessellation that seamlessly covers the globe. Node spacing is approximately 1° for the model presented here, but node spacing may be adjusted as needed. Velocity interfaces are defined by the radial distance from the center of the Earth, which allows us to explicitly build the GRS80 ellipsoid (Moritz, 1980) into the model and obviate travel time corrections for ellipticity.

We adopt the velocity versus depth profile in the crust from Pasyanos et al. (2004), which includes model layers for water, 3 types of sediments, upper crystalline crust, middle crust, and lower crust (Figure 2; Table 1). The crustal layers overlay a mantle velocity profile that is simplified to two parameters: velocity at the Moho and a linear velocity gradient with depth. The model parameterization in the mantle is a simplification of true mantle structure, but this parameterization has advantages for real-time computation of Pn travel times (see below). By interpolating model parameters from surrounding nodes – layer thickness, velocity, and mantle gradient – we generate a continuous model of the 3-D crust and laterally varying upper mantle.

Pn Travel Time Calculation

Parameterization of upper mantle velocity with a linear gradient facilitates an approximation for Pn travel time that enables real-time computation (~1 millisecond). Computation of Pn travel time at near-regional distance (<700 km) commonly assumes that the Pn phase propagates as a head wave, with a ray-path that follows the contour of the Moho (*e.g.* Hearn, 1984). The head wave assumption results in poor travel time prediction at far-regional distance (>~700 km) because the Pn ray can dive appreciably into the mantle due to a positive velocity gradient with depth and Earth sphericity (*e.g.* Zhao and Xie, 1993; Ritzwoller et al., 2003; Hearn et al., 2004). To more accurately predict Pn at far-regional distances, Zhao (1993) and Zhao and Xie (1993) employ a constant linear velocity gradient in the upper mantle for the whole study area.

The Zhao (1993) and Zhao and Xie (1993) travel time calculation is similar to the widely used approach of Hearn (1984), with an additional term (γ) introduced to account for diving rays (Figure 3). The travel-time calculation is

$$TT = \sum_{i=1}^{N} d_i s_i + \alpha + \beta + \gamma \qquad (1)$$

where d and s are the distance and slowness (taken as 1/velocity below the Moho) in each of the i segments comprising the great-circle path between Moho pierce points near the event and station, α and β are the crustal travel times at the source and receiver, and γ (described below).

We define α as:

$$\alpha = \sum_{j=1}^{M} \left[\sqrt{r_j^2 / v_j^2 - p^2} - \sqrt{r_{j+1}^2 / v_j^2 - p^2} \right] \qquad (2)$$

where v and r are the velocity and radius (from the center of the Earth to the top of the layer) for the M crustal layers from the event to the Moho (r_{M+1} is the radius of the Moho), and p is the spherical ray parameter.

We similarly define β as:

$$\beta = \sum_{k=1}^{N} \left[\sqrt{r_k^2 / v_k^2 - p^2} - \sqrt{r_{k+1}^2 / v_k^2 - p^2} \right] \qquad (3)$$

where v and r are defined as above for the N crustal layers from the station to the Moho.

From Zhao (1993),

$$\gamma = \frac{c^2 X_m^3}{24 V_0} \tag{4}$$

where X_m is the horizontal distance traveled in the mantle, and V_0 is a regional average of mantle velocity at the Moho. $c = g * s + 1/r$, where 1/r is an Earth flattening correction and r is the radius at which a ray enters and exits the linear velocity gradient, g (Helmberger, 1973; Zhao and Xie, 1993). This approximation is valid when $ch << 1$, where h is the bottoming depth of the ray in a linear velocity gradient.

We use a spatially varying mantle velocity gradient, *c* (Phillips et al., 2007), and we calculate γ by averaging *c* along the ray track. V_0 remains an average Pn velocity over the whole model, which allows us to take advantage of linear tomographic inversion methods (see below). Tests find that using a global average for V_0 introduces negligible travel-time error when Pn velocities range from 7.5 km/s to 8.3 km/s.

The Zhao and Xie (1993) method is applicable to events in the crust, making the approach well suited to nuclear explosion monitoring. However, seismic location algorithms may explore the possibility that an event occurred in the mantle, necessitating a consistent method of travel-time predictions for mantle events. For an event focus in the shallow mantle,

$$TT = \alpha + t_{mantle} \tag{5}$$

where α is the crustal travel time from the Moho to the station (as defined in (2)), and t_{mantle} is the travel time in the mantle. Fundamentally, travel times for two ray paths comprise t_{mantle}. One ray has endpoints at the Moho and passes through the event. The second ray is the subsection of the first ray that is entirely at depths below the event.

Adding or subtracting the component of the ray path below the event results in the ray leaving the event downward (+) or upward (-).

$$t_{mantle} = \frac{1}{2}\left(\left(\sum_{i=1}^{N} d_{mi}s_{mi} + t_x - \frac{c_m^2 x_m^3}{24V_0}\right) \pm \left(t_e - \frac{c_e^2 x_e^3}{24(V_0 + g_m z)}\right)\right) \qquad (6)$$

A derivation of (6) is provided in the Appendix, including variable definitions and physical depictions of some variables (Figure A1). See the Appendix for evaluation of travel time prediction accuracy.

Tomography

Starting Model

The model development domain here is Eurasia and North Africa, which we define as the region inside the latitude range of 0° to 90° and the longitude range of -20° to 150°. We set velocity profiles for nodes inside the development domain based on an *a priori* geophysical model. The method for determining geophysical regions and compiling velocity information for each region is described in Pasyanos et al. (2004), and the starting model is an update of the Pasyanos et al. (2004) model for latitude between 0° and 90° and longitude between -20° and 75°. Between longitudes 75° and 150°, we use an unpublished *a priori* model developed at Los Alamos National Laboratory (Steck et al., 2007). Outside of the development domain, we use a default velocity profile based on the *ak135* model (Kennett et al., 1995) for consistency with current monitoring practice. Expansion beyond Eurasia and North Africa does not require a change in the model parameterization itself, only modification of the velocity profile at each model node. Figures of the starting model are presented with the tomographic model for comparison.

Tomographic Formulation

The Pn travel time (Equation 1) lends itself to a linear tomographic formulation. Because our primary objective is to improve travel-time prediction, we avoid the use of parameters that would not be part of a subsequent travel-time calculation (*e.g.* event and station time terms). In matrix form, the tomographic system of equations is:

$$\begin{bmatrix} x_1^1 & \cdots & x_N^1 & -\frac{x_1^1 (X_m)^3}{24 V_o X_m} & \cdots & -\frac{x_N^1 (X_m)^3}{24 V_o X_m} & \sum_{p=1}^{Q} \frac{l_{1p}^1}{v_{1p}} & \cdots & \sum_{p=1}^{Q} \frac{l_{Np}^1}{v_{Np}} \\ \vdots & & & & \ddots & & & & \vdots \\ x_1^K & \cdots & x_N^K & -\frac{x_1^K (X_m)^3}{24 V_o X_m} & \cdots & -\frac{x_N^K (X_m)^3}{24 V_o X_m} & \sum_{p=1}^{Q} \frac{l_{1p}^K}{v_{1p}} & \cdots & \sum_{p=1}^{Q} \frac{l_{Np}^K}{v_{Np}} \\ & & & & & \text{Regularization} & & & \end{bmatrix} * \begin{bmatrix} s_1 \\ \vdots \\ s_N \\ c_1^2 \\ \vdots \\ c_N^2 \\ a_1 \\ \vdots \\ a_N \end{bmatrix} = \begin{bmatrix} t^1 \\ \vdots \\ t^K \\ \text{Regularization} \end{bmatrix} \quad (7)$$

where

t = *travel time*

s = *mantle slowness below the Moho (a.k.a. Pn slowness)*

x = *Pn distance (or weight) for each model node*

c = *normalized velocity gradient, v=vo(1+cz)*

X_m = *length of Pn ray path in the mantle*

Vo = *average Pn velocity*

v = *velocity of a crustal layer*

k = *index on K paths (travel-time observations)*

p = *index on Q crustal layers*

l = *length of the ray path in a specified crustal layer (determined by layer thickness and ray parameter in Equations (2) and (3)).*

a = *node-specific adjustment to the slowness of each crustal layer (crustal modifier).*

The tomographic equation solves for the model slowness below the Moho, *s* (a.k.a. Pn slowness), the square of mantle velocity gradient, c^2, and a scalar adjustment to crustal slowness, *a*. The formulation in Equation 7 is similar to the approach presented in Phillips et al. (2007), with the significant difference that we use a scalar adjustment to the slowness of the crustal stack, as opposed to a time term, to account for travel-time errors in crustal legs of the Pn ray. The crustal legs can impart as much or more error on the travel time prediction as the travel time in the mantle. Because our goal is to accurately predict subsequent travel times using the tomographic model, it is important to fold all adjustments affecting travel time into the model, rather than absorb the error in a time term that is discarded and will not be used in subsequent travel time prediction.

The tomographic inversion (solution to Equation 7) minimizes the misfit of squared travel-time residuals that are scaled by inverse arrival-time measurement uncertainty. Regularization of the system of equations takes the form of a Laplacian damping, which minimizes the curvature of the solution. Laplacian damping is applied independently to mantle slowness, mantle gradient, and the scalar adjustment to crustal slowness. The system is solved using a conjugate gradient method (Hestenes and Siefel, 1952).

Data Set

We combine bulletin data from the International Seismic Centre, U.S Geological Survey National Earthquake Information Center, and numerous regional networks across Eurasia into a reconciled database. To this database we have added tens of thousands of arrival-time measurements made at Lawrence Livermore and Los Alamos National Laboratories, as well as numerous detailed studies of event location. Epicenter accuracy for each event in the reconciled bulletin has been assessed using the network coverage criteria of Bondár et al. (2004). We further add non-seismic constraints based on known explosion locations, ground displacement from interferometric synthetic aperture radar (InSAR), as well as satellite imagery of man-made seismic sources. To diminish the possibility of introducing travel times for phases that interact with velocity discontinuities at ~410 km and ~660 km, the maximum event-station distance range is set to 15°. The minimum event-station distance range is determined by the post-critical refraction for a wave interacting with the Moho. In practice, the minimum distance varies from tens of km in the ocean (thin crust) to over 200 km in Tibet (thick crust).

Because the goal of this work is to produce a model for Pn travel time prediction for real-time monitoring, it is important that Pn prediction error is unbiased relative to teleseismic P wave prediction error. Previous efforts have achieved unbiased Pn error by using an *ad hoc* travel time correction (Yang et al., 2004). To achieve unbiased Pn error, we recomputed each event origin time in the tomography data using at least 10 P-wave arrivals. The hypocenter is then fixed during the tomographic procedure, which forces Pn prediction error to be unbiased relative to teleseismic P-wave error.

All picks are evaluated against an uncertainty budget that accounts for event mislocation, a global average of *ak135* prediction uncertainty, and arrival-time measurement uncertainty. We map the epicenter accuracy estimates to travel-time uncertainty using the formulation of Myers (2001).

$$\sigma_{\text{tepi}} = \frac{\partial t}{\partial \Delta} \frac{\sigma_{\text{epi}}}{2} \qquad [8]$$

where σ_{tepi} (seconds) is the standard deviation of travel time uncertainty attributable to epicenter uncertainty, σ_{epi} (km) is the standard deviation in epicenter error and $\partial t/\partial \Delta$ is the phase slowness (s/km). The factor of 2 accounts for random direction of event mislocation and a magnitude of mislocation that is distributed Gaussian. The total uncertainty for a given arrival time datum is the sum of uncertainty variance for event location, model-based travel time uncertainty (*e.g.* Flanagan et al., 2007) and arrival-time measurement uncertainty (σ^2_{meas}). Observations outside of the $3\sigma_{datum}$ bounds were removed.

$$\sigma_{\text{datum}} = \sqrt{\sigma^2_{\text{tepi}} + \sigma^2_{\text{model}} + \sigma^2_{\text{meas}}} \qquad [9]$$

In addition to data culling based on the datum-specific uncertainty budget, we also cull data based on a comparison of neighboring observations. This "local" outlier removal uses a kriging algorithm similar to the method outlined in Schultz et al. (1998). We gather all Pn residuals for a station and compute a geographic residual surface. The advantage of using the kriging method for interpolation is that we can also compute the point-specific uncertainty for residual prediction. Each residual is examined in the

context of the station-specific residual and uncertainty surfaces, and only data in the 2σ bounds of the residual surface are retained. We find that removal of local outliers better identifies residuals that are due to measurement uncertainty than outlier removal based on the distribution of all residuals.

Following removal of local outliers, we produce summary rays for each station. Arrival-time observations are again grouped by station, and residuals are plotted at the epicenter of the event. For each event, we count the number of neighboring events within 0.5° (the nominal bin size), and we order events by the count. Starting with the event having the highest count, we average residuals for all events within 0.5°, to produce a summary-ray travel time and an uncertainty estimate. Events comprising the summary ray are then discarded from the event list and the process is repeated on the event having the next highest count. This process is repeated until all events for that station are exhausted. From the ~600,000 Pn rays we produce ~162,000 summary rays. The dramatic reduction reflects paths that are repeatedly sampled in areas with high seismicity. Reduction of the data set by summary rays not only reduces the number of data (and therefore reduces the computational expense of the tomography) by approximately 70%, but the average datum uncertainty is reduced from 1.73 seconds to 1.28 seconds. The use of summary rays also mitigates sampling redundancy, which if left unaccounted, biases tomographic model adjustments to paths that are repeatedly sampled.

Data Coverage and Model Resolution

Figure 4 shows the node hit count for Pn rays throughout Eurasia, as well as the resulting tomographic "checkerboard" test for mantle-Moho velocity. The hit count is high

(~10,000) throughout the Tethys collision belt (a roughly east-west band from the Pyrenees through the Himalayas). Node hit count to the north of the Tethys collision is also good, with regional bulletins and peaceful nuclear explosions (PNEs) in the Former Soviet Union (Sultanov et al., 1999) providing data coverage. South of the Tethys collision hit count is poorer. Some regions are not sampled by any Pn ray (i.e. North Africa), and the tomographic model is unaltered from the starting model in these regions.

Checkerboard resolution tests show that the model is well resolved in regions having a higher hit count. Regions with high hit count tend to have more crossing paths and a better mix of long and short paths, which are needed to resolve mantle velocity at the Moho and the velocity gradient. This result highlights the success of the anomaly recovery in regions of good data coverage and the importance of the starting model in regions with poorer data coverage.

Results

Figure 5 shows maps of the tomographic model. The general tectonic features that are present in the starting model are also seen in the tomographic model (Figure 5a). Low-velocity anomalies in the Mediterranean region, Red Sea Rift, and Iranian Plateau remain in the RSTT model, but the velocities are even lower. While the starting model correctly identifies the average velocity over broad regions, the RSTT model shows that structure varies appreciably within these tectonic provinces. In the Scandinavian region, mantle velocity at the Moho increases to values in excess of 8.3 km/s. The Atlantic ridge is better defined by a sinuous low velocity anomaly after tomography. Moving east, the starting and RSTT models are in broad agreement across the Siberian Plateau, with some

small areas (*e.g.* immediately east of the Ural Mts.) of increased velocity. The largest difference between the starting and RSTT models is along the Pacific subduction zone. The starting model does not include low velocity in the mantle wedge above the subducted oceanic slabs, whereas the slowest mantle P-wave velocities in the RSTT model are above these subducted slabs. The starting model includes low mantle velocities throughout China, whereas the RSTT model suggests that mantle velocity in eastern China is even slower than the starting model, and velocity in western China – including the Tibetan Plateau – is close to the global average. The Hindu Kush and the Tien Shan Mountains are clearly resolved to be localized areas of low mantle velocity.

Mantle velocity gradient tends to be highest in convergence zones. The tomography map of mantle gradient (Figure 5b) shows a strong gradient along the Tethys convergence zone. Similarly, the mantle velocity gradient is high under the Pacific subduction zones, where the slow velocities of the wedge transition to the fast slab. True mantle structure in the convergence zones is clearly not as simple as the linear gradient that we image in this study, but the results presented here are consistent with downgoing (cold) material at the convergence zones. The linear gradient does, however, capture the effect of the structure on travel time to first order. The starting model has broad regions of strong mantle gradient across northern Eurasia, which is largely unchanged in the RSTT model. Change in the crustal modifier (a in Equation 7) from the starting model is small, despite relatively light damping on the a parameters.

Improvement in travel time prediction.

We leave out 10% of the tomographic data for use in non-circular validation tests. The validation data provides sampling across Eurasia, so residual summary statistics are a good measure of expected model performance in monitoring systems. Figure 6 shows residual distributions for *ak135*, the starting model, and the RSTT model. Recalling that origin times are determined by minimizing teleseismic P-wave residuals relative to *ak135* predictions, it is perhaps surprising that Pn error for the *ak135* model has a median value of 0.31 seconds. Median Pn error for the starting model is also 0.31 seconds. For the RSTT model, median Pn error is reduced to 0.16 seconds, a 48% reduction from the *ak135* model. The Pn residual standard deviations (mean removed) relative to the *ak135*, starting model, and RSTT model are 1.99 sec., 1.99 sec., and 1.58 sec., respectively.

We use an interquartile measurement to compute a robust estimate of standard error for Pn prediction (Figure 7). Figure 7 includes the *ak135* error vs. distance curve, as well as the curve for the starting and RSTT models. The uncertainty vs. distance curve for the starting model and *ak135* are similar at near-regional distance. *ak135* uncertainty increases more rapidly with distance than does starting model uncertainty, and the starting model uncertainty is ~0.2 seconds lower than *ak135* at far-regional distance. The RSTT model is significantly improved over both *ak135* and the starting model, with a relatively consistent error vs. distance of approximately 1.25 seconds. The RSTT model reduces error by 0.5 to 1.0 seconds relative to *ak135*. We note that a nominal one-second measurement (pick) error variance was subtracted from the measured residual variance before plotting (see Flanagan et al., 2007). For instance, the plotted value of 1.25 seconds (variance of 1.56 s^2) was derived from an observed residual error of 1.6 seconds.

Location Tests

Figure 8 is a map of the events used in relocation tests. None of these events was used in the tomography and each of these events is either an explosion with an accurate location, or an earthquake that is surrounded by a local network (*i.e.*. GT5 criteria of Bondár et al., 2004). These events are well distributed geographically, providing a representative sampling of location performance across the modeling region. Each event is located using Pn arrival times only. We use the LocOO code (Ballard, 2002), which is based on the single-event location method outlined in Jordan and Sverdrup (1981). Uncertainty ellipses were computed using the method of Evernden (1969), where "coverage" ellipse axes are scaled by *a priori* (input) model and pick uncertainties. For travel-time prediction uncertainties we use the distance-dependant curves in Figure 7, and either an analyst estimate of pick uncertainty or a nominal 1-second uncertainty. Because event depth is poorly constrained with a Pn data set, event depths are fixed. These events were selected partially because a large number of Pn arrival times are available for each event. We relocated the events using 4, 8, 16, and 32 Pn arrivals. Data selection was random and we created 10 realizations of each case (number of Pn arrivals). Results presented below are an average of the 10 realizations.

Table 2 summarizes epicenter error when the *ak135*, starting, and RSTT models are used for travel-time prediction in the location algorithm. The results are also summarized in the Figure 9a. Figure 9a shows that median epicenter error for the RSTT model is significantly lower than for *ak135* and the starting model, regardless of the number of Pn arrivals. Further, the RSTT model reaches a relatively constant level of epicenter error at

~9 km with only 8 Pn arrivals, whereas a stable level of epicenter error at ~17 km for *ak135* and the starting model is reached after 16 Pn arrivals are used.

Table 3 summarizes ellipse area for *ak135*, the starting model, and the RSTT model, when 4, 8, 16, and 32 Pn arrivals are used. The primary difference between the results for the *ak135* and starting models is that there are fewer outliers with enormous ellipse area for the starting model than for *ak135* (i.e. the "tail" of the distribution is shorter). Ellipses for the RSTT model are consistently smaller than for the other two models. Ellipse sizes (case with 16 Pn arrivals) are also summarized in Figure 9b,c. Figure 9b is a semilog plot of median ellipse area vs. the number of Pn phases, showing that ellipses for the RSTT model are significantly smaller than for the *ak135* or the starting model. Figure 9c shows that the percentage of uncertainty ellipses with area less than 1000 km^2 is far greater for locations determined with the RSTT model. The 1000 km^2 metric is taken from the Comprehensive Nuclear Test Ban Treaty (CTBT), which allows for an on-site inspection search area of 1000 km^2. The results show that with 4 to 8 Pn arrivals, none of the uncertainty ellipses are expected to be less than 1000 km^2, when either the *ak135* model or the starting model are used. Even using 32 Pn arrivals results in only ~23% of uncertainty ellipses with area less than 1000 km^2, when *ak135* or the starting model are used. Using the RSTT model, it is possible to achieve the 1000 km^2 goal with only 4 Pn arrivals, although the network configuration must be ideal. With 16 Pn arrivals approximately one-half of the events meet the 1000 km^2 goal, and with 32 Pn arrivals ~88% of ellipses meet the 1000 km^2 goal.

Figure 10a shows that coverage ellipses are representative of true location error when the assessments of model error (Figure 7) are input to the location algorithm. The expected

number of ground-truth events occurs inside the ellipses of varying confidence level. Figure 10b shows the reduction in error ellipse size for the case with 16 Pn arrivals.

Combining Pn and P Data

While low-magnitude events are expected to record more reliably at regional distance than at teleseismic distance, a small number of teleseismic (P) recordings may be expected even for events between magnitude 3 and 4. For a small event it is important to include all available data to achieve a network with the smallest possible gap in event-station azimuthal coverage. Therefore, we test epicenter accuracy when both Pn and P data are used to determine the location. In these tests *ak135* is used for P-wave travel time calculations, and *ak135*, the starting model, and the RSTT model are each tested for Pn travel time calculations.

For each of the nuclear explosions in the test data set, we use all available Pn data. We then add P-wave arrivals into the location data set. For each test case the number of P arrivals is varied from 50% to 400% of the number of Pn arrivals, or until P-wave data are exhausted. In each test case we present the median epicenter error for 10 random realizations of the P-wave data set. Figure 11 shows that when the RSTT model is used for Pn travel time predictions and the *ak135* model is used for P predictions, epicenter estimates are measurably more accurate than cases where either *ak135* or the starting model is used for Pn travel time predictions. In most cases epicenter accuracy tends to converge as more P data are used, because the location solution is dominated by *ak135* predictions of P-wave travel times. The exceptions are the 2006 Korean nuclear test and the 1990 nuclear test in the Former Soviet Union event. For the Korean event, epicenter

error becomes exceedingly small for the RSTT model (~1 km), and for the Soviet event, regional travel time errors are large enough that the locations are significantly biased even when large numbers of teleseismic data are used. In all cases in which Pn data outnumber or are equal in number to teleseismic data, epicenter accuracy for the RSTT model is equal to or better than epicenter accuracy when the *ak135* model is used for Pn travel time prediction.

Conclusions

Reduction of seismic monitoring thresholds requires the use of regional seismic data to constrain event locations. One-dimensional (radially symmetric) models that are almost universally used in real-time monitoring cannot account for the geologic complexity of the crust and upper mantle. We develop a Regional Seismic Travel Time (RSTT) model and method to account for the first-order effects of crust and upper mantle structure on regional travel times. The model parameterization is a global tessellation with node spacing of approximately 1°, with a velocity vs. depth profile at each node. Layer depths and velocities are interpolated to generate a 3-D crustal model, overlaying laterally varying velocity in the upper mantle. Velocity profiles in the mantle include a velocity at the Moho and a linear gradient as a function of depth. The linear gradient parameterization allows application of an analytical approximation that accounts for a Pn ray that dives below the Moho into a linear velocity gradient (Zhao and Xie, 1993; Phillips et al., 2007). Due to this approximation, Pn travel times can be computed in approximately 1 millisecond, which highly desirable for operational monitoring systems.

We adapt tomographic methods to the model RSTT parameterization and use a data set of approximately 600,000 Pn arrivals to improve travel time prediction accuracy across Eurasia and North Africa. Tests show that RSTT Pn travel time prediction accuracy is improved to approximately that of the teleseismic P-wave, which is the benchmark phase in seismic monitoring. We confirm that the reduction in travel time prediction error also improves location accuracy (Figure 9). Using 16 Pn arrivals, epicenter error is improved from a median value of 17.3 km (*ak135*) to 9.3 km with the RSTT model. The area of epicenter uncertainty ellipses is reduced from a median value of 3070 km^2 (*ak135*) to 994 km^2 (Figure 10). Importantly, in tests using 16 Pn arrivals, 51% of the ellipse areas are smaller than the 1000 km^2 allowed under the CTBT for on-site inspection, as opposed to 0% of ellipse with area less than 1000 km^2 for the *ak135* model. Of particular note, Figure 9c shows that few epicenter uncertainty ellipses are expected to meet the 1000 km^2 goal when either the *ak135* model or the starting model is used. Using the RSTT model, it is possible to achieve the 1000 km^2 goal with only 4 Pn arrivals, although the network configuration must be ideal. Using 32 Pn arrivals ~88% of ellipses meet the 1000 km^2 goal.

The RSTT model brings the Pn travel-time prediction accuracy down to the level of prediction accuracy for teleseismic P, which is the primary phase used in global monitoring. As a result, the RSTT approach enables the use of regional Pn arrival times in seismic monitoring systems without degrading location performance. RSTT is presented as a first step beyond the use of a 1-D base model in operational monitoring systems. While the base model provides the primary travel time calculation, travel time

corrections that are based on fully 3-D models or empirical travel times can and should be used to further improve prediction accuracy. While the RSTT model is global in extent, the crucial tomographic optimization is currently limited to Eurasia and North Africa; however, we plan to apply RSTT tomography to North America and eventually to the globe. Last, we have extended RSTT travel-time calculation to Sn, Pg, and Lg phases, and we will report on the travel time calculation and model development for computation of these later phases in a future publication.

Data and Resources

Most of the arrival-time measurements used in this study can be obtained from the International Seismic Centre (ISC). Bulletin arrival times include the EDR catalog (http://earthquake.usgs.gov/regional/neic), the ISC catalog (http://www.isc.ac.uk), the REB catalog prior to 2002 (http://www.pidc.org), the EHB catalog (ftp://ciei.colorado.edu/pub/user/engdahl/EHB), and the FINNE (http://www.seismo.helsinki.fi/bul/index.html), all of which are publicly available. Additional arrival-time measurements were made by researchers at the Air Force Technical Applications Center, Lawrence Livermore National Laboratory, and Los Alamos National Laboratory; these measurements are not presently available to the public. Measurements made at LLNL and LANL were made using waveform data obtained through the Incorporated Research Institutes in Seismology (IRIS) Data Management Center (DMC) at www.iris.edu, the U.S. National Data Center (USNDC) at www.tt.aftac.gov, GEOSCOPE at geoscope.ipgp.jussieu.fr, IIEES at www.iiees.ac.ir, GEOFON at geofon.gfz-potsdam.de, and MEDNET at mednet.rm.ingv.it. Other data

were obtained directly from networks in Azerbaijan, Georgia, Israel, Jordan, Kazakhstan, Kuwait, Oman, Saudi Arabia, Turkey, and United Arab Emirates. Plots were made using the Generic Mapping Tools (GMT) version 4.2.0 (Wessel and Smith, 1998; www.soest.hawaii.edu/gmt).

Acknowledgements

We thank the Office of Nuclear Detonation Detection (NA-222) within the National Nuclear Security Administration for funding this effort. David Russell provided critical guidance in the formative stages of the RSTT project. Leslie Casey provided useful comments and suggestions. This work was performed under the auspices of the U.S. Department of Energy by Lawrence Livermore National Laboratory under contract No. DE-AC52-07NA27344.

References.

Ballard, S. (2002). Seismic Event Location Using Levenberg-Marquardt Least Squares Inversion, Sandia National Laboratories Report, SAND2002-3083.

Bondár, I., S. Myers, E. R. Engdahl, and E. Bergman (2004). Epicenter accuracy based on seismic network criteria, *Geophys. J. Int.,* **156,** no. 3, 483–496.

Buland, R. and C. Chapman (1983). The computation of seismic travel times, *Bull. Seism. Soc. Am*., **73**, 1271-1302.

Crotwell, H.P., T.J. Owens, and J. Ritsema (1999), The TauP ToolKit: Flexible seismic travel-time and raypath utilities, *Seism. Res. Lett.*, **70**, 154-160.

Dziewonski, A., and F. Gilbert (1976). The effect of small, aspherical perturbations on travel time and a re-examination of the corrections for ellipticity, *Geophys. J. R. Astr. Soc*., **44**, 7-17.

Engdahl, E.R., R. van der Hilst, and R. Buland (1998). Global Teleseismic Earthquake Relocation with Improved Travel Times and Procedures for Depth Determination, *Bull. Seism.. Soc. Am.,* **88**, 722-743.

Evernden, J. F. (1969). Precision of epicenters obtained by small numbers of world wide stations, *Bull. Seism. Soc. Am*., **59**, 1365-1398.

Flanagan, M.P., S.C. Myers, and K.D. Koper (2007). Regional travel-time uncertainty and seismic location improvement using a three-dimensional a priori velocity model, *Bull. Seismolog. Soc. Am*., **97**, 804-825.

Hearn, T. M. (1984). Pn travel times in southern California, *Jour. Geophys. Res*., **89**, 1843-1855.

Hearn, T.M., S. Wang, J.F. Ni, Z. Xu, Y. Yu, and X. Zhang (2004). Uppermost mantle velocities beneath China and surrounding regions, *J. Geophys. Res*., **109**, B11301, doi:10.1029/2003JB002874.

Helmberger, D.V. (1973). Numerical seismograms of long-period body waves from seventeen to forty degrees, Bull. Seismol. Soc. Am., 63, 633-646, 1973.

Herrin, E., W. Tucker, J. Taggart, D. Gordon, and J. Lobell (1968). Estimation of surface focus P travel times, *Bull. Seism. Soc. Am.,* **58**, 1273-1291.

Hestenes, M.R., and E. Stiefel (1952). Methods of conjugate gradients for solving linear systems, *J. Res. Nat. Bur. Stand*., **49** (6).

Jeffreys, H., and K. E. Bullen (1940). Seismological Tables, *Br. Assoc. for the Adv. of Sci*., London, 1940.

Johnson, M., and C. Vincent (2002). Development and testing of a 3-D velocity model for improved event location: A case study for the India-Pakistan region, *Bull. Seism. Soc. Amer*., **92**, 2893-2910.

Jordan, T.H., and K.A. Sverdrup (1981). Teleseismic location techniques and their application to earthquake clusters in the south-central Pacific, *Bull. Seism. Soc. Am*., **71**, 1105-1130.

Kennett, B.L.N. and E.R. Engdahl (1991). Traveltimes for global earthquake reference location and phase identification, *Geophys. J. Int,* **105**, 429-465.

Kennett, B.J.N., E.R. Engdahl and R. Buland (1995). Constraints on seismic velocities in the Earth from traveltimes, *Geophys. J. Int,* **122**, 108-124.

Lomax, A., J. Virieux, P. Volant and C. Berge (2000), Probabilistic earthquake location in 3-D and layered models: Introduction of a Metropolis-Gibbs method and

comparison with linear locations, in Advances in Seismic Event Location, Thurber, C.H., and N. Rabinowitz (eds.), Kluwer, Amsterdam, 101-134.

Moritz, H. (1980). Geodetic reference system 1980. Bull. Geodesique. Paris, **54** (3).

Morozov, I. B., E. A. Morozova, S. B. Smithson, P. G. Richards, V. I. Khalturin, and L. N. Solodilov (2005). 3-D First-Arrival Regional Calibration Model of Northern Eurasia, *Bull. Seism. Soc. Amer*., **95**, 1535-1560, doi: 10.1785/0120040087.

Myers, S. C. (2001). Methods of travel-time residual declustering for the Knowledge Base Calibration and Integration Tool (KBCIT), *Lawrence Livermore National Laboratory Report*, 14 pp., UCRL-ID-142521**.**

Myers, S. C., and C. A. Schultz (2000). Improving Sparse Network Seismic Location with Bayesian Kriging and Teleseismically Constrained Calibration Events, *Bull. Seism. Soc. Am.,* **90**, 199-211.

Pasyanos, M.E., W.R. Walter, M.P. Flanagan, P. Goldstein, and J. Bhattacharyya (2004). Building and testing an a priori geophysical model for western Eurasia and North Africa, *Pure. And Applied Geophys*., **161**, 235-281.

Phillips, W.S., M.L. Begnaud, C.A. Rowe, L.K. Steck, S.C. Myers, M.E. Pasyanos, and S. Ballard (2007). Accounting for lateral variations of the upper mantle gradient in Pn tomography studies, *Geophys. Res. Lett*., **34**, doi:10.1029/2007GL029338, 2007.

Ritzwoller, M.H., M.P. Barmin, A. Villasenor, A.L. Levshin, and E.R. Engdahl (2002). Pn and Sn tomography across Eurasia to improve regional seismic locations, *Tectonophysics*, **358**, 39-55.

Ritzwoller, M. H., N. M. Shapiro, A. Levshin, E. A. Bergman, and E. R. Engdahl (2003). The ability of a global 3-D model to locate regional events, *J. Geophys. Res.* **108,** 2353, doi 10.1029/2002JB002167.

Schultz , C.A., S.C. Myers, J. Hipp, and C. Young (1998). Nonstationary Bayesian kriging: a predictive technique to generate corrections for detection, location, and discrimination, *Bull. Seism. Soc. Am.,* **88**, 1275-1288.

Steck, L. K., C. A. Rowe, M. L. Begnaud, W. S. Phillips, V. L. Gee, and A. A. Velasco (2004), Advancing seismic event location through difference constraints and three-dimensional models, *paper presented at 26th Seismic Research Review* - Trends in Nuclear Explosion Monitoring, Orlando, Florida.

Sultanov, D. D., J. R. Murphy, and Kh. D. Rubinstein (1999). A seismic source summary for Soviet peaceful nuclear explosions, *Bull. Seismol. Soc. Am.* **89**, 640–647.

Yang, X., I. Bondár, J. Bhattacharyya, M. Ritzwoller, N. Shapiro, M. Antolik, G. Ekstro¨m, H. Israelsson, and K. McLaughlin (2004). Validation of Regional and Teleseismic Travel-Time Models by Relocating Ground-Truth Events, *Bull. Seism. Soc. Amer*., **94**, 897–919.

Zhao, L.-S. (1993). Lateral variations and azimuthal isotropy of Pn velocities beneath Basin and Range province, *Jour. Geophys. Res*., **98**, 22,109-22,122.

Zhao, L.-S., and J. Xie (1993). Lateral variations in compressional velocities beneath the Tibetan Plateau from Pn traveltime tomography, *Geophys. J. Int*., **115**, 1070-1084.

Appendix: Calculating travel times for mantle events

Zhao and Xie (1993) and Zhao (1993) provide a derivation for Pn travel time approximation in equations (1) and (4) for events in the crust. We extend the approximation for events originating in the mantle. Figure A1 shows that extending the Zhao and Xie (1993) approximation to an event in the mantle involves manipulation of two constituent ray paths. The first constituent ray starts at the Moho and travels downward, passing through the event, and ending at the recording station (*whole path ray*). The travel time for the portion of the *whole path ray* in the mantle (*whole mantle ray*) is calculated directly from Zhao and Xie (1993). The second constituent ray is the portion of the *whole-path ray* that is entirely below the event (*sub-event path*). Using the travel times for the *whole path* and the *sub-event ray*, we can compute the travel time for a mantle-focus event. The difficulty lies in specifying the *whole path* and *sub-event rays*.

Following Zhao and Xie (1993) and Zhao (1993) the travel time for the *whole mantle ray* is

$$t_{wm} = t_m + \gamma_m = t_m - \frac{c_m^2 x_m^3}{24 V_m}, \tag{A1}$$

where t is travel time, γ is the gradient portion of the travel time (negative), c is the normalized gradient, x is the horizontal distance, V is velocity, the m subscript signifies evaluation at or along the Moho, and the subscript wm is signifies whole mantle.

The travel time for the *sub-event ray* is

$$t_{se} = t_e + \gamma_e = t_e - \frac{c_e^2 x_e^3}{24 V_e} = t_e - \frac{c_e^2 x_e^3}{24(V_m + g_m z)}, \quad \text{(A2)}$$

where the subscript *e* signifies evaluation at or along the depth of the event, and the subscript *se* signifies sub-event.

From the geometry in Figure A1, the travel time from the event to the Moho pierce point beneath the station (the desired quantity) can be computed as a combination of t_{wm} and t_{se}.

$$t_{mantle} = \left(t_{wm} \pm t_{se}\right)/2, \quad \text{(A3)}$$

where ± depends on whether the ray leaves the event upwards (-) or downwards (+).

Determining the whole mantle ray

In order to use A3 we must find the *whole mantle ray*. We first define the horizontal distance traveled by the *whole mantle ray*, x_m. In a linear velocity gradient, the bottoming depth of the ray, *h*, and x_m are uniquely related. From Figure A1, the distance measured along the Moho from the event to the point where the ray pierces the Moho, *d*, is,

$$d = \left(x_m \pm \frac{r_m x_e}{\left(r_m - z\right)} \right)/2, \quad \text{(A4)}$$

where x_e is the horizontal distance of the sub-event path. The ± indicates when the ray is up-going (-) or down-going (+), r_m is the radius from the center Earth to the Moho at the event, and *z* is the depth of the event below the Moho. Using Equation A3 from Zhao (1993)

$$x_m = \left(2/c_m\right)\sqrt{\left(1 + c_m h\right)^2 - 1} \quad \text{(A5)}$$

$$x_e = (2/c_e)\sqrt{\left(1 + c_e(h - z)\right)^2 - 1}, \tag{A6}$$

We determine h by substituting A5 and A6 into A4 (simplifying $r = r_m/(r_m - z)$), and minimizing the difference between the distance (d) computed by A1. In practice, we minimize $\log_{10}$ of the squared difference using Brent's method:

$$\log\left(\left(\sqrt{(1 + c_m h)^2 - 1} - r\frac{c_m}{c_e}\sqrt{\left(1 + c_e(h - z)\right)^2 - 1} - dc_m\right)^2\right) \text{ (up-going)}, \tag{A7}$$

$$\log\left(\left(\sqrt{(1 + c_m h)^2 - 1} + r\frac{c_m}{c_e}\sqrt{\left(1 + c_e(h - z)\right)^2 - 1} - dc_m\right)^2\right) \text{ (down-going)}, \tag{A8}$$

and use the misfit to determine whether the ray is up-going or down-going. The values for x_m and x_e, which depend on the Moho pierce point, are recalculated using an updated ray parameter for the turning-point depth (h), and the procedure is iterated to convergence.

Computing normalized gradient and travel time

Once the values of x_m and x_e are determined, we can be substituted into A1 and A2 to compute the travel time for the *whole-mantle ray* and the *sub-event ray*, and we can use A3 to compute the mantle portion of the travel time for the event of interest. The following clarifies details of the calculation. The head-wave travel time along the Moho is simply a sum of the slowness multiplied by the incremental distances as in equation (1), with an additional component for the Moho travel time beyond the source-receiver distance (t_x) (see Figure A1).

$$t_x = \frac{x_m - d}{V_m} \tag{A9}$$

A head-wave travel time along the event depth path is determined using the path-averaged velocity at depth *z*.

$$t_e = \frac{x_e}{V_m + g_m z} \tag{A10}$$

The normalized gradient *c* in A1 and A2 vary slightly depending on whether the purpose of the calculation is to find the turning point depth *h* or the gradient portions of the travel times. When determining *h* in equations A4-A8, the normalized gradient uses the path-averaged velocity.

$$c_m = \frac{g_m}{V_m} + \frac{1}{r_m} \tag{A11}$$

$$c_e = \frac{g_m}{V_e} + \frac{1}{r_e} = \frac{g_m}{V_m + g_m z} + \frac{1}{r_e} \tag{A12}$$

When calculating the gradient portions of the travel times in A1-A3 and A11-A12, we substitute a regional average of the Moho velocity V_0 for V_m, in order to keep travel times consistent with crustal events and the tomography.

$$c_m = \frac{g_m}{V_0} + \frac{1}{r_m} \tag{A13}$$

$$c_e = \frac{g_m}{V_0 + g_m z} + \frac{1}{r_e} \tag{A14}$$

The full travel time for a mantle event becomes:

$$t_{mantle} = \frac{1}{2}\left(\left(\sum_{i=1}^{N} d_{mi}s_{mi} + t_x - \frac{c_m^2 x_m^3}{24V_0}\right) \pm \left(t_e - \frac{c_e^2 x_e^3}{24(V_0 + g_m z)}\right)\right), \tag{A15}$$

which can also be separated into head-wave and gradient components:

$$t_{head} = \frac{1}{2}\left(\sum_{i=1}^{N} d_{mi}s_{mi} + t_x \pm t_e\right) = \frac{1}{2}\left(\sum_{i=1}^{N} d_{mi}s_{mi} + \frac{x_m - d}{V_m} \pm \frac{x_e}{V_m + g_m z}\right) \tag{A16}$$

$$t_{gradient} = -\frac{1}{48}\left(\frac{c_m^2 x_m^3}{V_0} \pm \frac{c_e^2 x_e^3}{V_0 + g_m z}\right) \tag{A17}$$

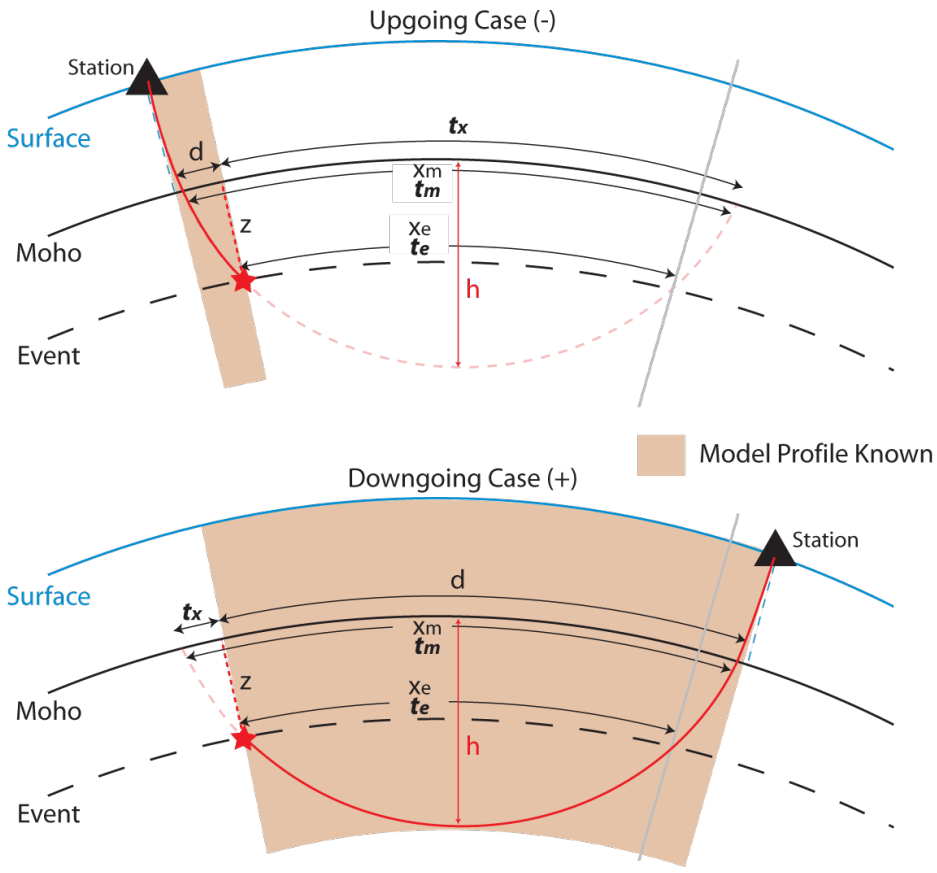

Figure A1: Geometry and variable definition extending the Zhao and Xie

(1993) formulation to events in the shallow mantle. The red star is the event location and the triangle is the station location. The theoretical projected portion of the ray path is shown as a muted dashed red line. Note that horizontal distances are evaluated in a flat earth, and Appendix equations correct for Earth sphericity.

Validity of the Zhao and Xie (1993) approximation

Zhao (1993) assumes that the product of the normalized mantle velocity gradient, *c*, and the bottoming depth of the ray traveling in the linear velocity gradient, h, is much less than 1 (i.e. ch<<1). We test the accuracy of the calculation using a model with the ak135 crust and Moho velocity (Kennett et al., 1995), overlain by a mantle with a linear velocity gradient. Test cases include gradients of 0.000, 0.001, 0.003, and 0.005 km/s/km (Figure A2). As expected the error approximately follows the contour of *ch*. The goal of a computational error of less than 0.2 seconds is approximately met when *ch* <0.12. We note that tomographic procedures will force the travel time to agree with observations, and therefore meet the goal of this project, which is improved travel time predictions for monitoring. We caution that *ch* should be carefully assessed before model velocities are interpreted.

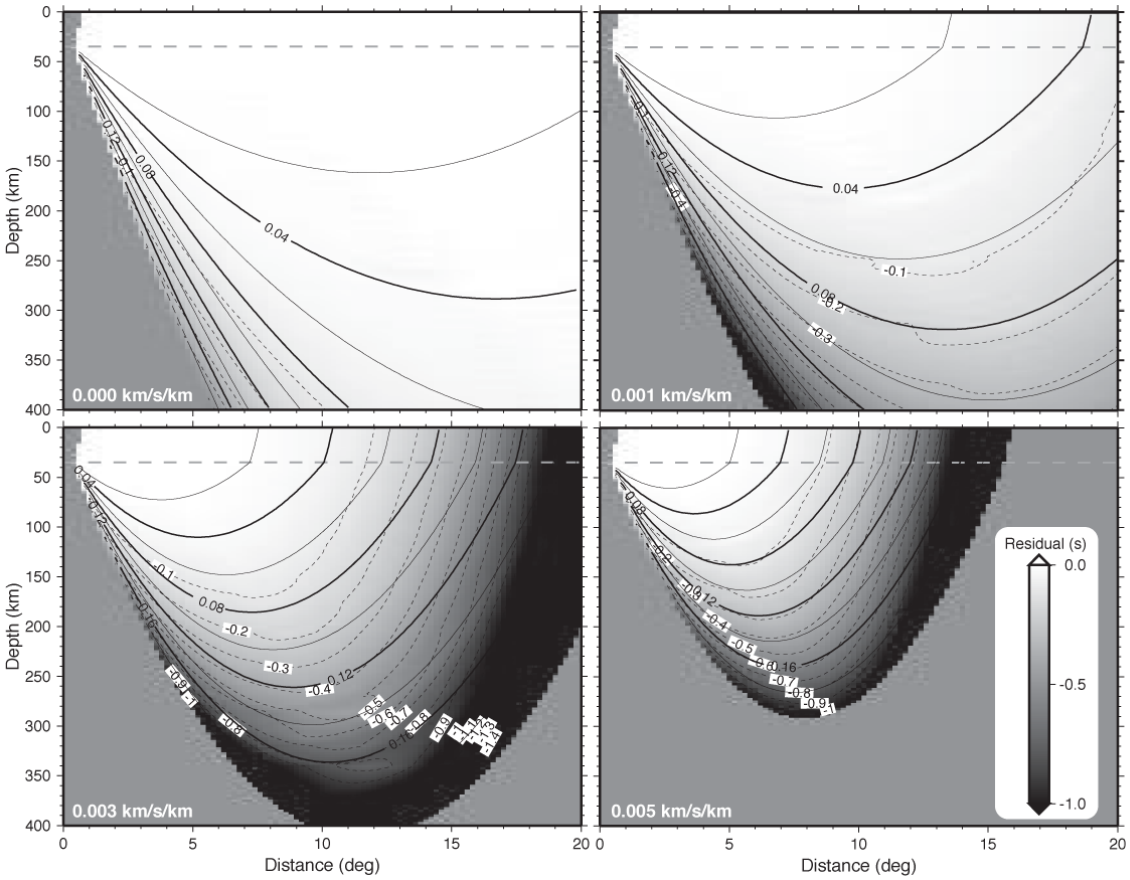

Figure A2: Travel time differences between formulation above and the TauP toolkit (Crotwell et al., 1999) for varying mantle gradient values. The *ak135* crust and velocity at the Moho were used in each model. Only the gradient is varied. The solid lines are contours of equal *ch* values (see text). Dotted contour lines are of equal residual value, with an interval of 0.1 s.

Tables:

Table 1. Definition of model entities that are used to construct depth profiles at each model node. Depths define the bottom of the layer. The top of a layer is implicitly the bottom of the overlaying layer. Mantle gradient is unique in that it is not a layer.

Entity number	Model entity	Representation	Parameter
1	Water	Layer	Velocity
2	Sediment 1	Layer	Velocity
3	Sediment 2	Layer	Velocity
4	Sediment 3	Layer	Velocity
5	Upper Crust	Layer	Velocity
6	Middle Crust	Layer	Velocity
7 (Moho ⇓)	Lower Crust	Layer	Velocity
8	Mantle @ Moho	Half Space	Velocity
9	Mantle Gradient		Gradient

Table 2. Epicenter error summary statistics.

	Median (km)				90th percentile (km)			
Number of Pn data	4	8	16	32	4	8	16	32
ak135	31.6	22.5	17.3	15.6	141.7	199.2	89.2	53.4
Starting Model	21.7	18.1	16.8	15.0	76.0	55.2	33.3	32.8
Tomography (RSTT) Model	14.4	9.3	9.3	8.2	40.4	23.3	20.9	21.1

Note: results for locations with station azimuthal gap less than 180°.

Table 3. Epicenter uncertainty ellipse summary statistics

	Median (km^2)				90th percentile (km^2)			
Number of Pn data	4	8	16	32	4	8	16	32
ak135	19,042	7,502	3,070	1,423	218,310	20,731	6,790	3,730
Starting Model	13,900	5,704	2,738	1,432	40,947	14,129	5,114	3,962
Tomography (RSTT) Model	3,297	1,765	994	478	4,843	2,549	1,490	1,018

Note: results for locations with station azimuthal gap less than 180°.

Figures

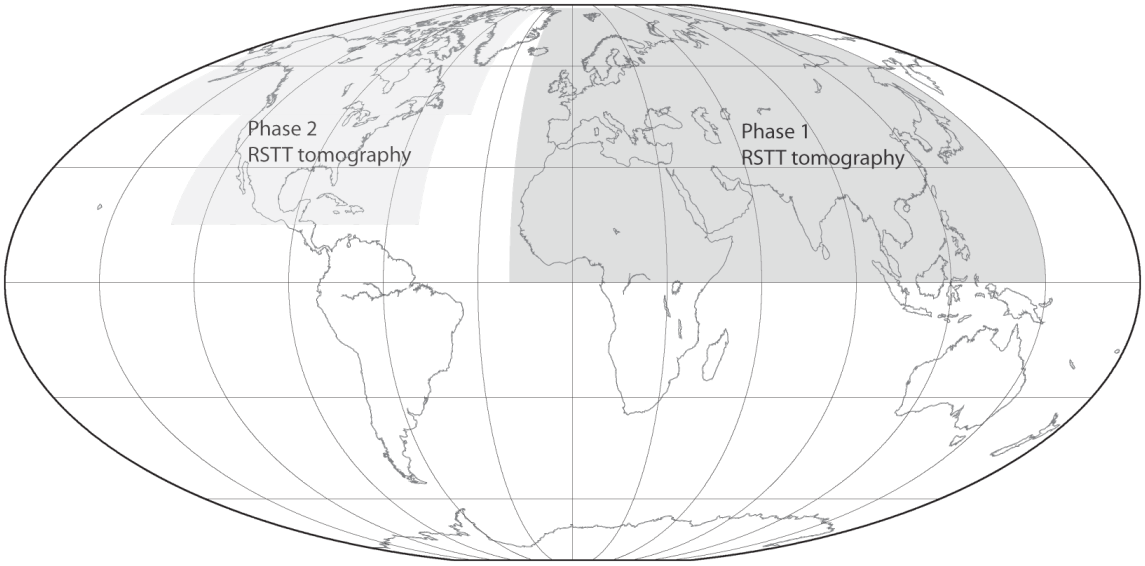

Figure 1. Phased approach for applying RSTT tomography, with the end goal of producing a global model for the universal prediction of regional phases.

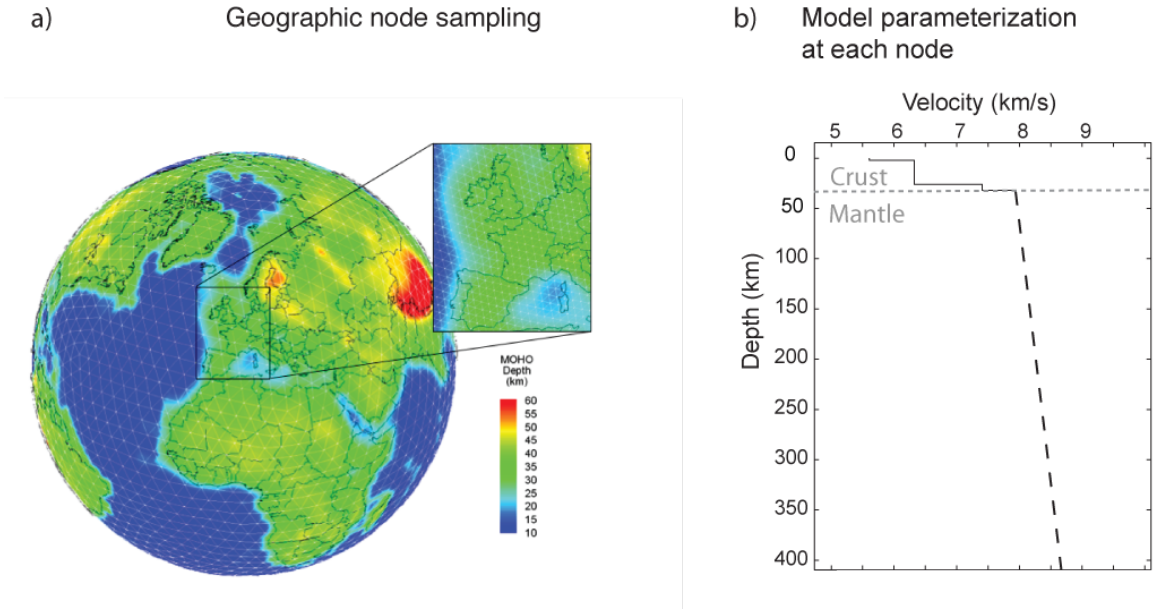

Figure 2. Global model parameterization. a) An example tessellation with approximately 5° grid spacing. The inset shows the 1° used in this study. Color indicates Moho depth of the starting model. b) An example velocity/depth profile as defined at each node. The mantle portion of the profile is specified by the velocity at the crust/mantle interface and a linear gradient.

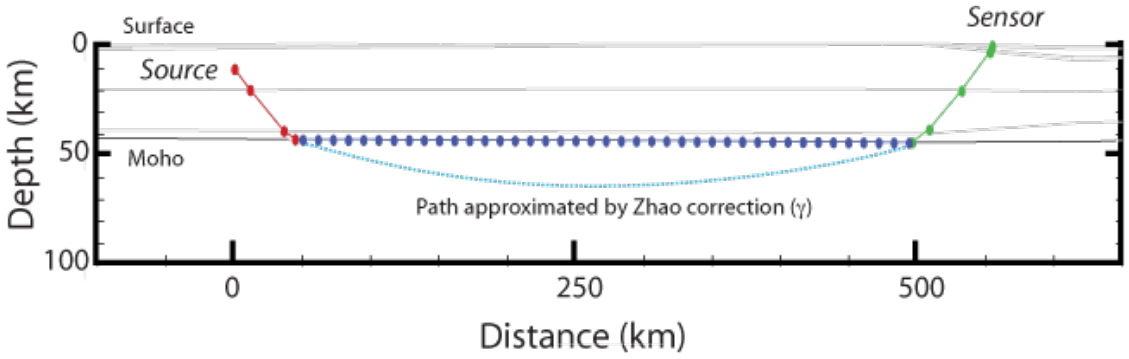

Figure 3. Cross section extracted from the laterally variable model. This example shows crustal layers (grey), and how crustal layers can pinch out. The variable-depth Moho is also shown. The first, second, third, and fourth terms of the Pn travel-time calculation [Eqn 1] are colored blue, red, green and cyan, respectively.

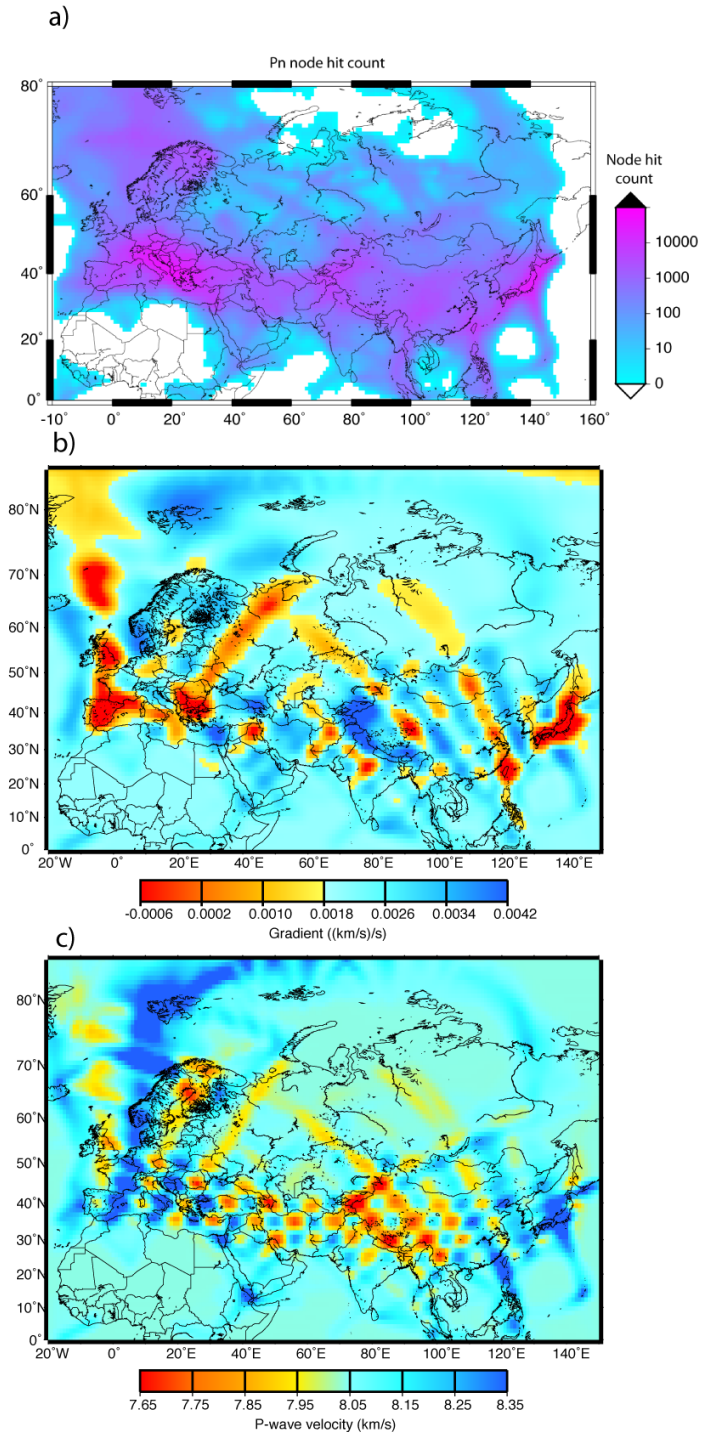

Figure 4. a) Node hit count for Pn rays. Nodes hit count exceeds 10,000 throughout the Tethys convergence zone and Scandinavia. Hit count varies across northern Eurasia from tens of hits down to a few. North Africa and some ocean areas are devoid of data. b) Tomographic checkerboard test for the mantle velocity gradient (~1000 km squares). c) Tomographic checkerboard test for the mantle velocity at the Moho (~500 km squares).

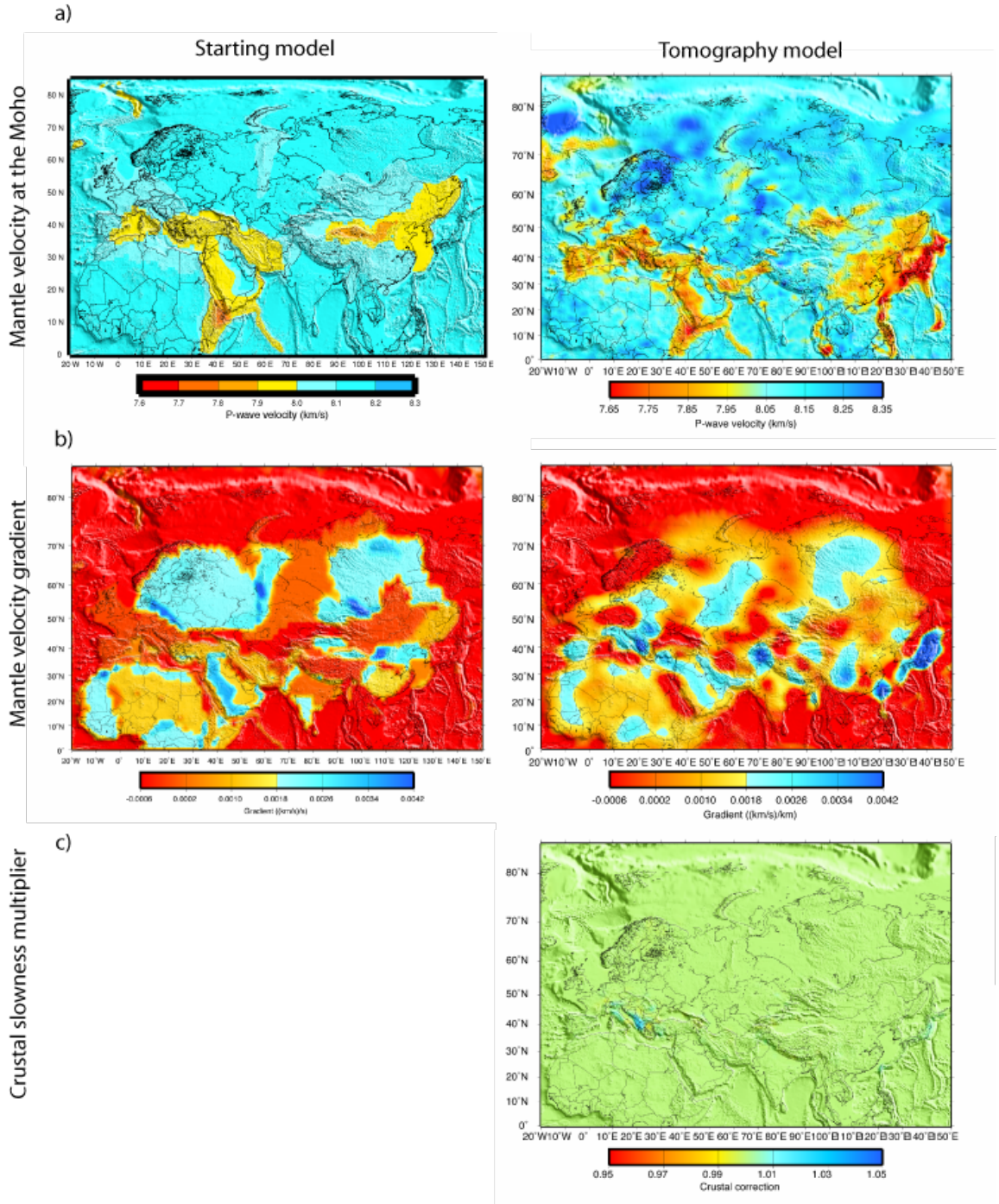

Figure 5. Comparison of starting and RSTTs. a) Velocity below the Moho. b) Mantle gradient (km/s/km). c) Tomographic crustal modifier (*a* in Equation 7).

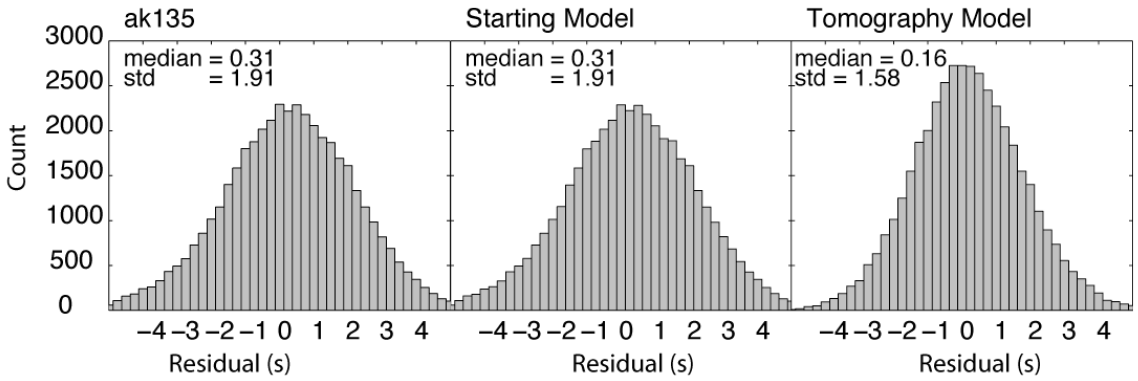

Figure 6. Travel-time residual histograms for a validation data set (not used in the tomography). The model is listed above each histogram, and summary statistics are provided in the upper left.

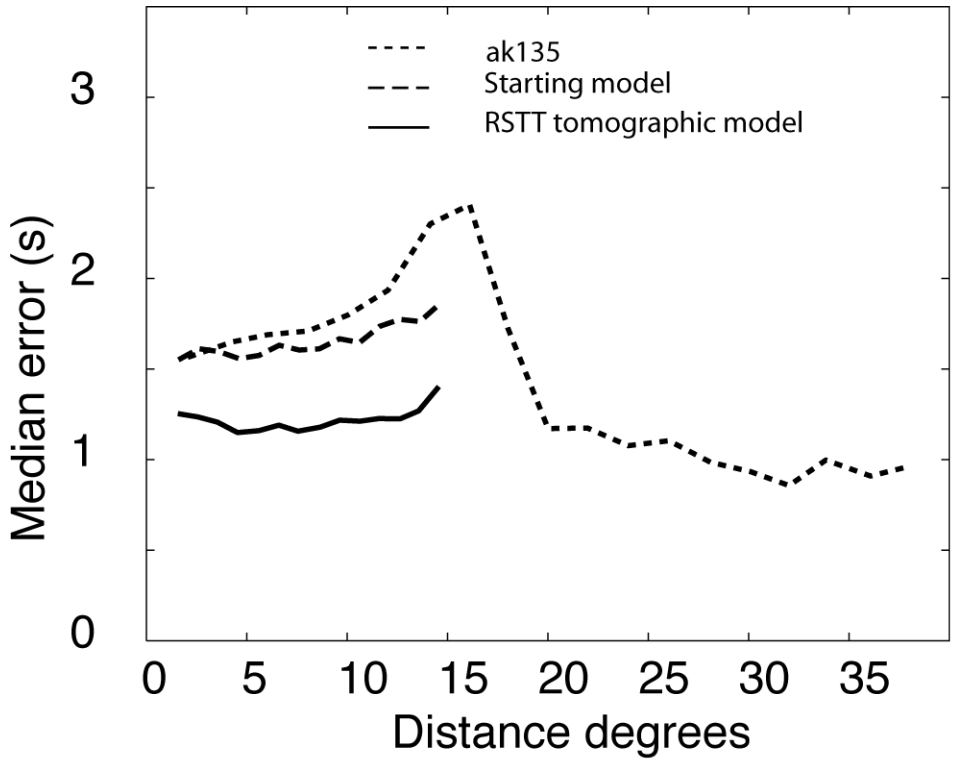

Figure 7. Travel-time error as a function of distance. The median residual in 1° distance bins is plotted for each model.

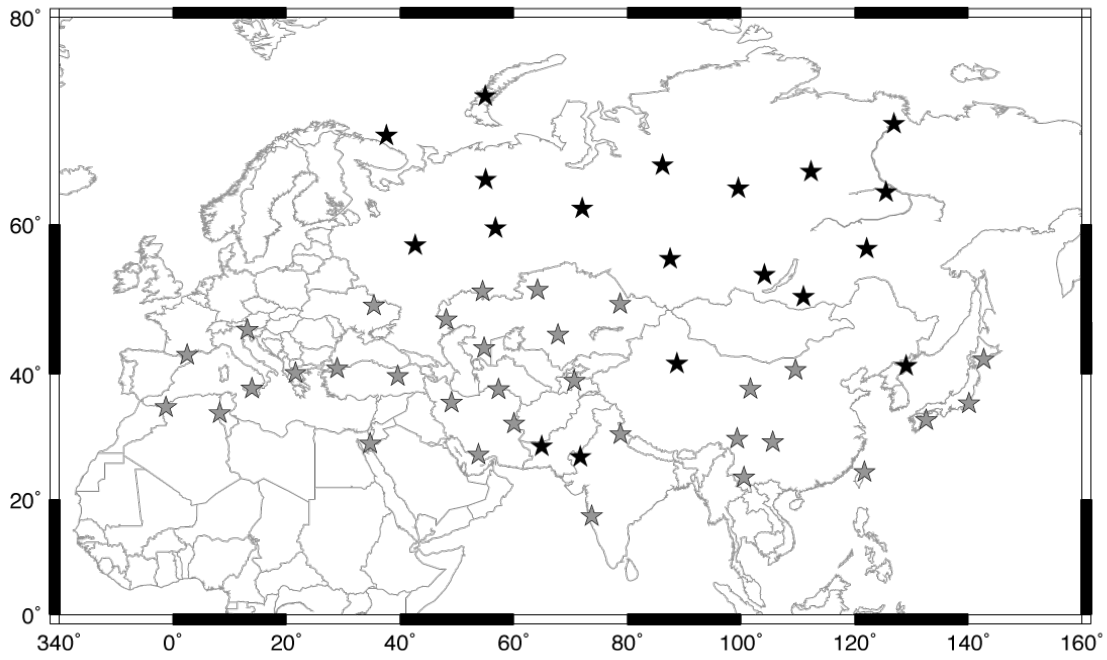

Figure 8. Validation data set used for location. The grey stars are GT5 epicenters, and the black stars are explosions with accurate epicenters.

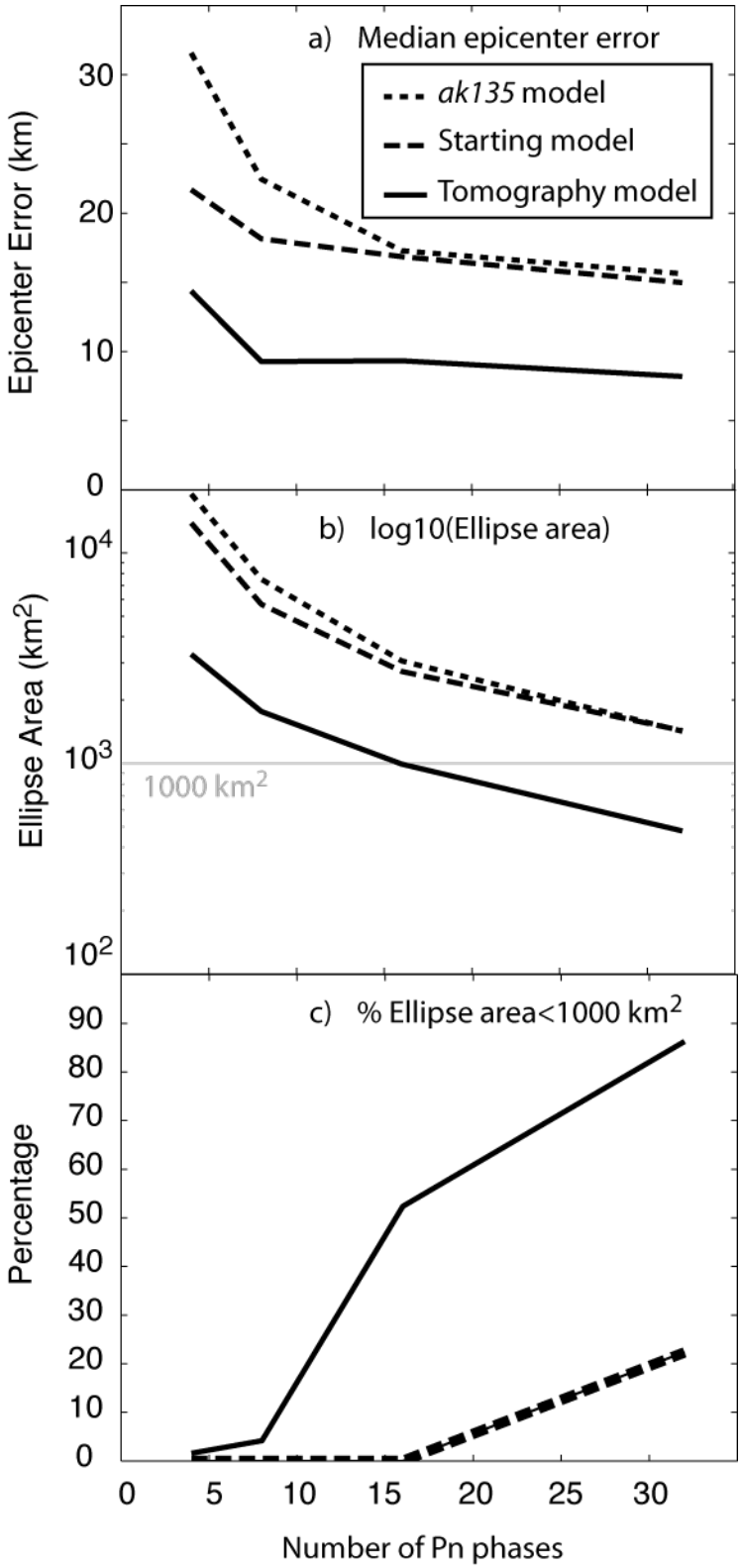

Figure 9. (a) Epicenter error, (b) semilog plot of median ellipse area, and (c) percentage of coverage ellipses with area < 1000 km^2. In (a), (b), and (c) parameters are plotted vs. number of Pn data used in the location. Starting model and ak135 overlap in (c).

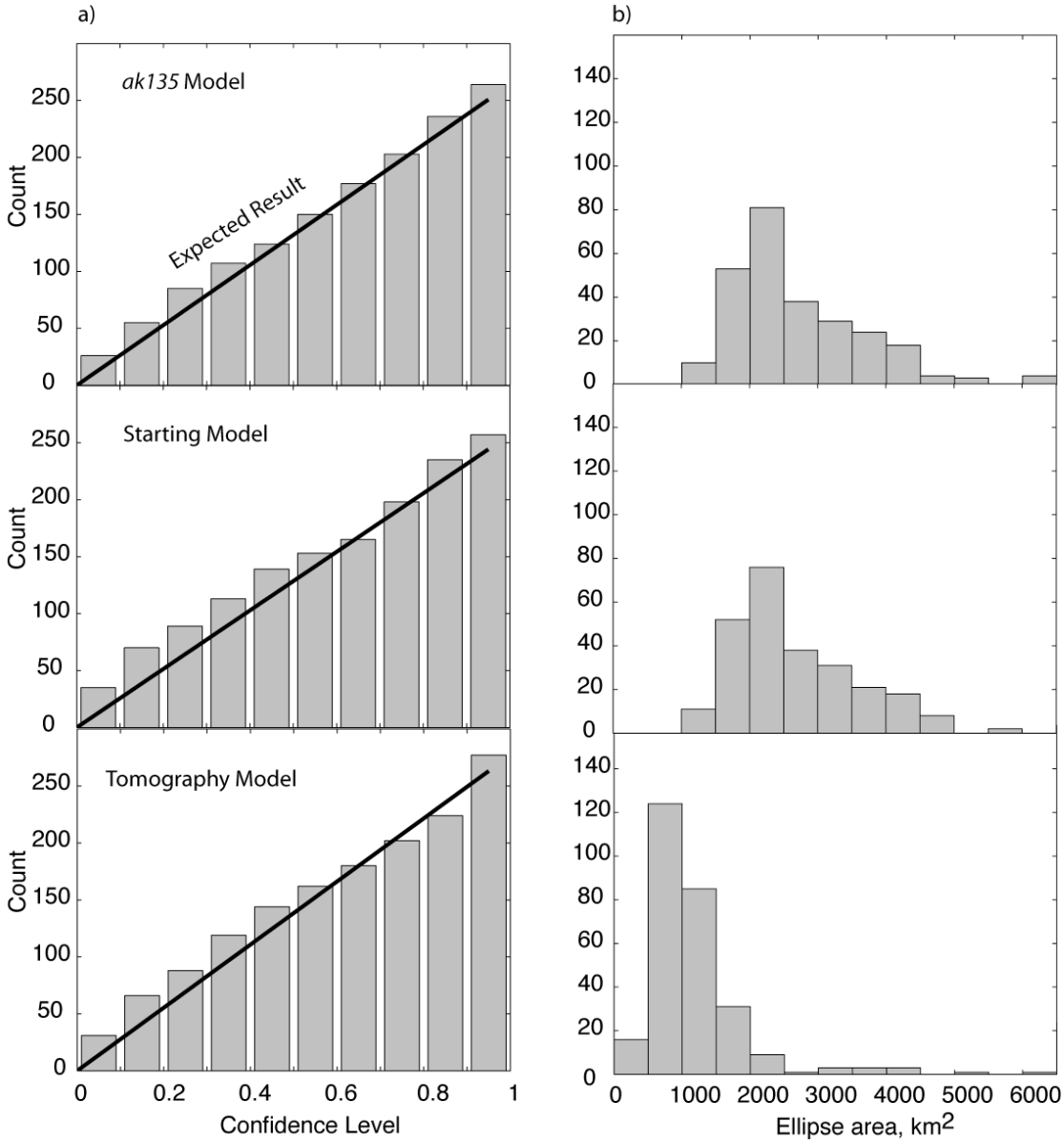

Figure 10. (a) Epicenter ellipse validation and (b) reduction in ellipse area for locations constrained with 16 Pn data. a) Histograms show the number of ground-truth epicenters occurring within ellipses of varying confidence level. The expectation is that 10% of events will fall within the 10% confidence ellipse, 20% within the 20% confidence ellipse, etc. The red line shows the expected trend of the histogram if ellipses accurately depict epicenter error. b) Histograms show the occurrences of ellipse area for the *ak135* model, starting model, and RSTT.

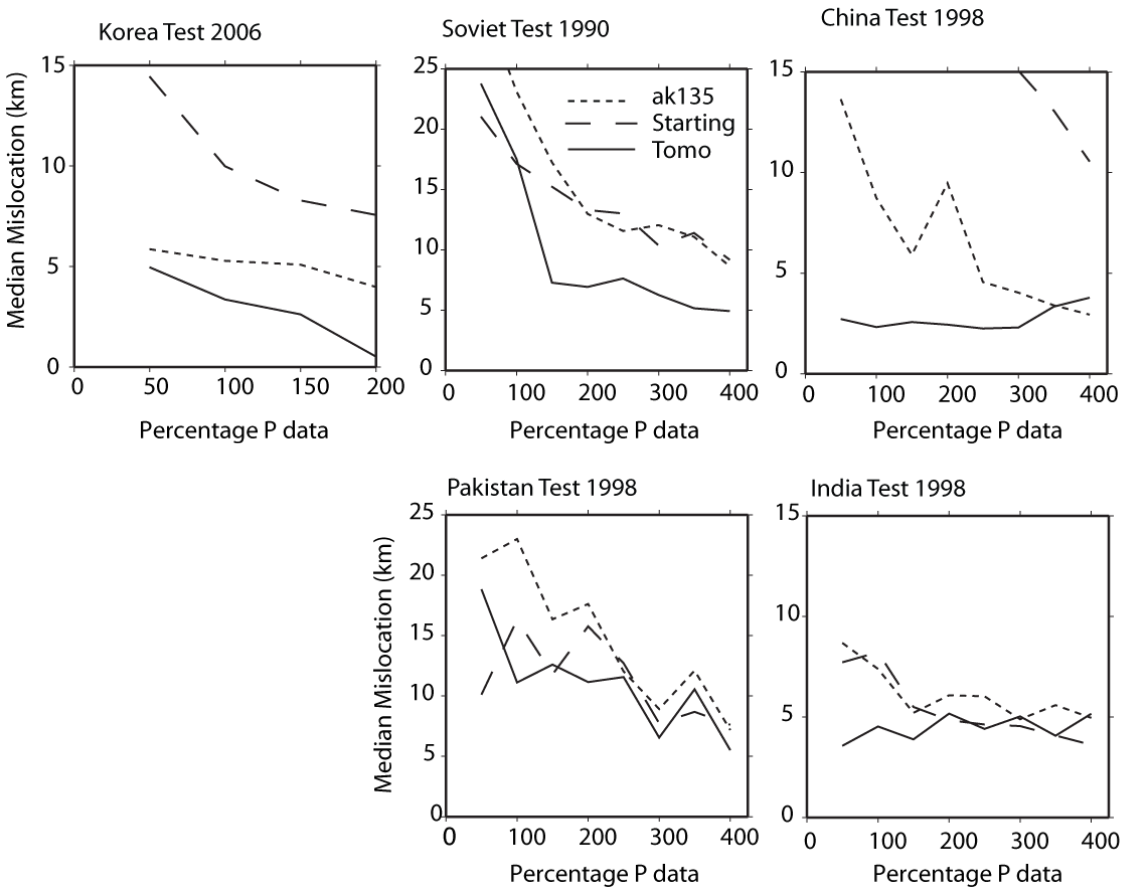

Figure 11. Epicenter accuracy with mixed Pn/P data sets. All Pn arrivals are used. Each plot shows the influence of adding (teleseismic) P arrivals and using the ak135 model to predict P travel times. The abscissa is computed as the number of P arrivals divided by the number of Pn arrivals times 100. Median epicenter error for 10 realizations is plotted.